Controlled synthesis of a Ni_2 dual-atom catalyst for synergistic CO_2 electroreduction

Xiang-Ming Liang [1], Hong-Juan Wang [1], Chao Zhang, Di-Chang Zhong, Tong-Bu Lu [*]

Institute for New Energy Materials & Low Carbon Technologies, School of Materials Science and Engineering, Tianjin University of Technology, Tianjin 300384, China

ABSTRACT

Dual-atom catalysts (DACs) have drawn much attention recently by virtue of the synergistic effect within the dual-atom sites, while controlled synthesis of pure DACs remains a challenge. Herein, a uniform dual-atom Ni_2 catalyst (Ni_2-NCNT) was controllably synthesized using a dinuclear Ni complex as the precursor, in which directly bonded Ni_2 pairs are uniformly anchored on N-doped carbon nanotubes. Ni_2-NCNT exhibits extraordinary catalytic activity, selectivity and stability for electroreduction of CO_2 into CO, with a partial current density for CO (j_{CO}) of 76 mA cm^{-2}. The j_{CO} mass activity of Ni_2-NCNT is 2.3-times higher than that of corresponding Ni_1-NCNT single-atom catalyst. DFT calculations reveal that the synergistic coordination of *COOH at the Ni_2 dual-atom site can dramatically lower the reaction free energy for *COOH formation, thus promoting the CO_2 electroreduction.

1. Introduction

The energy shortage resulting from the limited fossil fuel resources and the climate change induced by the excessive CO_2 emission are critical problems restricting the sustainable development of human society [1–3]. Electrocatalytic CO_2 reduction is an attractive strategy to overcome these issues, enabling CO_2 to be utilized as a chemical feedstock and be converted into useful fuels or chemicals [4–14]. Large catalytic current and high Faradaic efficiency (FE) are required before CO_2 electroreduction comes to practical use. However, in aqueous electrolytes, hydrogen evolution reaction would proceed within a similar cathodic potential regime, which could substantially lower the selectivity towards CO_2 reduction along with the increase of current densities [15–18]. Few electrocatalysts with high FEs under large current densities have been reported, and the design and synthesis of electrocatalysts featuring both high current density and FE remains a major challenge [19–21]. In the last decade, single-atom catalysts (SACs) have attracted much attention because of their high atomic utilization and excellent catalytic activity in a wealth of reactions [22–28]. However, owing to the single-site nature, they are generally not as competent for complex multi-step reactions such as CO_2 reduction reaction (CO_2RR) [29–32].

It has been found that the coordination environment of active sites plays a vital role for electrocatalytic activity and selectivity of CO_2 reduction via changing the reaction energy barriers [19,23,33] and the electrochemical route [11,28]. Dual-atom catalysts (DACs), with an additional metal active center introduced near the single-atom site, have drawn much attention recently by virtue of the synergistic effect within the dual-atom sites [33–45], which can change the adsorption configuration of reactants and intermediates, thereby reducing the reaction free energies [33]. As a result, DACs usually exhibit higher catalytic performance compared with corresponding SACs. Moreover, DACs offer a unique perspective for revealing the structure–performance relationship at the atomic level [46–48]. Therefore, it is highly desirable to develop new strategies for controlled synthesis of highly pure DACs, which, however, still remains a great challenge. Thus far, only a few strategies (such as atomic layer deposition [49–51] and wet chemical reduction [52–57]) have been reported. The routine method of synthesizing DACs is to increase the probability of pairing between metal atoms by simply elevating their concentration. However, the controllable synthesis of highly pure DACs via the above routine method is rather difficult, because it is inevitable to form a mixture of SAC and DAC, and metal atoms are also prone to agglomerate [46]. Therefore, it is highly desirable to develop a controllable strategy for the fabrication of pure DACs to accurately understand the synergy mechanism.

Herein, a highly pure Ni_2 DAC of Ni_2-NCNT was controllably synthesized via pyrolysis a mixture of a dinuclear complex Ni_2(qpyzc)$_2$ with carbon nanotubes (CNTs) and dicyandiamide under 600 °C (H_2qpyzc = 8-quinoline-1*H*-pyrazole-3-carboxamide). The dinuclear complex precursor effectively fixes the Ni_2 dual-atom sites during pyrolysis process, thus rendering this synthesis method highly reproducible. The obtained Ni_2-NCNT can take advantage of the synergy between two adjacent Ni

---

atoms as active centers to exhibit outstanding CO$_2$RR catalytic performance, with a high FE for CO above 90% over a wide potential range from −0.8 V to −1.2 V vs. RHE, a large partial current density for CO (76 mA cm^{-2} at −1.40 V vs. RHE), and a high electrocatalytic stability. Density functional theory (DFT) calculations reveal that the Ni$_2$ site in Ni$_2$-NCNT can significantly lower the reaction free energy of *COOH intermediate for promoting the CO$_2$ electroreduction.

2. Experimental section

2.1. Materials

Purified water (18.25 MΩ·cm) used in all the experiments was produced from a Water Purifier (UPR-II-10T). All chemicals used were of the highest purity available from commercial sources without any further purification.

2.2. Synthesis of H$_2$qpyzc (8-quinoline-1H-pyrazole-3-carboxamide)

Triphenyl phosphite (1.55 g, 5 mmol), tetrabutyl ammonium bromide (1.61 g, 5 mmol), 1H pyrazole-3-carboxylic acid (0.56 g, 5 mmol) and 8-aminoquinoline (0.72 g, 5 mmol) were heated at 120 °C for 1 h under careful stirring. Then cold MeOH (10 mL) was added to the viscous reaction mixture and stirred for 30 min. A light-yellow precipitate formed, and was filtered off and then washed with cold MeOH. Yield: 774 mg, 65%.

2.3. Synthesis of H$_2$qpyrc (N-(quinolin-8-yl)-1H-pyrrole-2-carboxamide)

The ligand was obtained with a synthesis method similar to that for H$_2$qpyzc; 1H pyrrole-2-carboxylic acid (0.56 g, 5 mmol) was used as the starting material instead of 1H pyrazole-3-carboxylic acid. Yield: 714 mg, 60%.

2.4. Synthesis of Ni$_2$-NCNT

CNT (40 mg), H$_2$qpyzc (1.25 mg) were dispersed in EtOH (20 mL), and the solution was agitated with sonication for 10 min. The MeOH solution (5 mL) containing Ni(CH$_3$COO)·4H$_2$O (2.5 mg) was then added into the above system, and the mixture was refluxed for 4 h under vigorous stirring. The samples with dinuclear complexes loaded on CNT were obtained after centrifugation, and then washed and dried in vacuum at 40 °C. A small porcelain boat containing dicyandiamide (200 mg) was placed in a larger magnetic boat along with the dried black powder. Then, the boat was heated at 600 °C under Ar atmosphere for 2 h at a rate of 5 °C min^{-1}. The obtained product was dispersed in hydrochloric acid (0.1 M, 20 mL) and stirred for 10 h, and then washed with H$_2$O and EtOH. Ni$_1$-NCNT was dried in vacuum at 40 °C for 12 h.

2.5. Synthesis of Ni$_1$-NCNT

The Ni$_1$-NCNT was obtained with a synthesis method similar to that for Ni$_2$-NCNT. H$_2$qpyrc (1.25 mg) was used as the starting material instead of H$_2$qpyzc. The samples with mononuclear complexes loaded on CNT were obtained after rotary evaporation and dried in vacuum at 40 °C. Other reactants and synthesis procedure were the same as that for Ni$_2$-NCNT.

2.6. Synthesis of NCNT

A small porcelain boat containing dicyandiamide (200 mg) was placed in a larger magnetic boat along with the dried CNT (40 mg). Then, the boat was heated at 600 °C under Ar atmosphere for 2 h at a rate of 5 °C min^{-1}. The obtained product was washed with H$_2$O and EtOH. NCNT was dried in vacuum at 40 °C for 12 h.
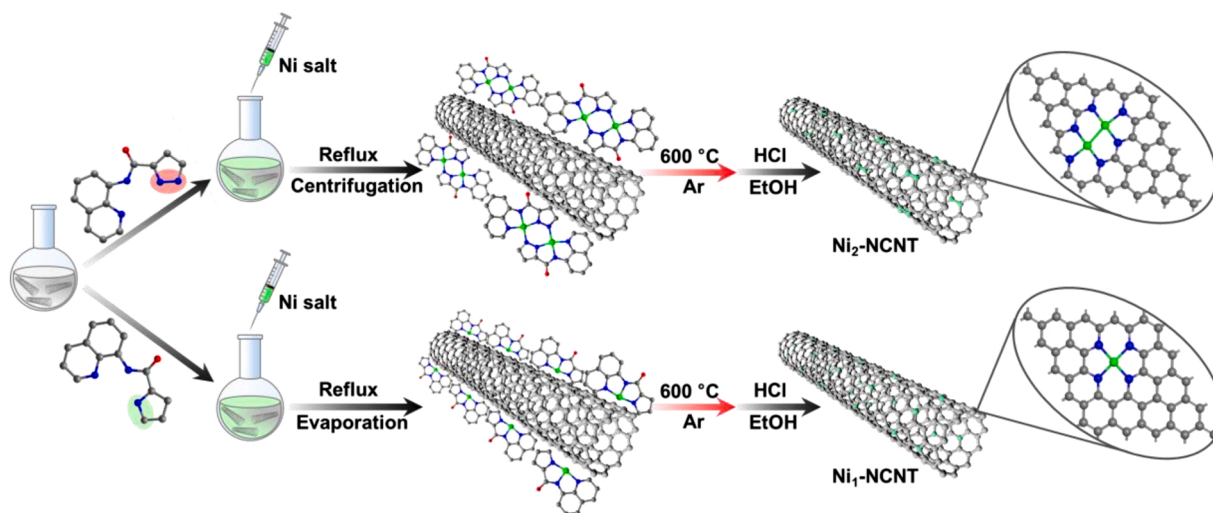
3. Results and discussion

3.1. Synthesis and structural characterization

Dinuclear complexes have well defined molecular structures, and thus could ideally serve as the precursor for the synthesis of DACs. Under proper conditions, the coordination bonds between metal centers and the organic ligand could effectively stabilize the diatomic metal pair, and thus prevent the metal atoms from agglomeration during the pyrolysis process, which could enable the precise and controllable synthesis of DACs. In this work, the organic ligands H$_2$qpyzc and H$_2$qpyrc were synthesized according to the reported methods (H$_2$qpyzc = 8-quinoline-1H-pyrazole-3-carboxamide, H$_2$qpyrc = N-(quinolin-8-yl)−1H-pyrrole-2-carboxamide) [58], and their structures were confirmed via ^{1}H nuclear magnetic resonance (NMR) analysis (Figs. S1 and S2). Fig. S3 illustrates the molecular structure of the dinuclear complex Ni$_2$(qpyzc)$_2$, and Fig. S4 shows the powder X-ray diffraction (XRD) pattern of the synthesized Ni$_2$(qpyzc)$_2$. Owing to the poor solubility of Ni$_2$(qpyzc)$_2$, it is rather difficult to use the conventional method of physical mixing to ensure the Ni$_2$(qpyzc)$_2$ molecules to be evenly distributed on the surface of CNTs. Therefore, we adopted the strategy of in situ synthesis. As shown in Scheme 1, by adjusting the ligands (H$_2$qpyzc or H$_2$qpyrc), the dinuclear or mononuclear complex was in situ generated on CNTs, respectively, and the corresponding DAC or SAC was obtained after pyrolysis. First, the solid powders of the ligand and CNTs were dispersed in ethanol, and the resulting suspension was subsequently heated to 60 °C. Ni(CH$_3$COO)$_2$·4H$_2$O (dissolved in methanol) was added into the above suspension, and the mixture was refluxed for 4 h. The dinuclear Ni complexes formed in situ could be readily anchored onto the CNTs, resulting in a more even distribution. The solid mixture was collected via centrifugation and washed with water and ethanol. The in situ formed dinuclear complexes on CNTs were verified via XRD. As shown in Fig. S5, diffraction peaks belonging to dinuclear complex and CNTs could be found with a Ni$_2$(qpyzc)$_2$/CNT feeding ratio ≥ 8%; as the content of the complex decreases, the peaks of dinuclear complex become less prominent. Upon heating Ni$_2$(qpyzc)$_2$/CNT composite to 600 °C in Ar atmosphere, the N-coordinated Ni$_2$ dual-atom sites were formed on CNTs with dicyandiamide used as a nitrogen source. Finally, dilute hydrochloric acid and ethanol were used to remove the nanoparticles and organic impurities that could have formed. For comparison, the SAC counterpart (denoted as Ni$_1$-NCNT) was synthesized in a similar way using H$_2$qpyrc to instead of H$_2$qpyzc, and N-doped carbon nanotubes (denoted as NCNT) were also synthesized via direct pyrolysis of CNTs with dicyandiamide as the nitrogen source under 600 °C.

In the Raman spectra of NCNT, Ni$_1$-NCNT and Ni$_2$-NCNT (Fig. S6a), the peaks located at 1336 and 1570 cm^{-1} are assigned to chaotic sp^3 carbon (D band) and graphitic sp^2 carbon (G band), respectively, confirming the formation of graphitized structures and carbon defects in these catalysts. From the value of I_D/I_G, it can be seen that Ni$_1$-NCNT and Ni$_2$-NCNT are more defect-rich than NCNT, which probably results from the Ni doping. The XRD patterns of NCNT, Ni$_1$-NCNT and Ni$_2$-NCNT show peaks at 25.5° and 42.7°, which are assigned to the (002) and (100) planes of graphitic carbon, respectively, and the peaks corresponding to Ni nanoparticles are not found (Fig. S6b). N$_2$ adsorption analysis shows the Brunauer–Emmett–Teller (BET) surface areas of Ni$_1$-NCNT and Ni$_2$-NCNT are comparable (Fig. S7a). Both Ni$_1$-NCNT and Ni$_2$-NCNT show almost identical CO$_2$ adsorption capacities, which are significantly higher than that for NCNT due to the Ni doping (Fig. S7b).

The microscopic structures of Ni$_1$-NCNT and Ni$_2$-NCNT were examined via high-resolution transmission electron microscopy (HRTEM), scanning electron microscopy (SEM), and high-angle annular dark-field scanning transmission electron microscopy (HAADF-STEM). The HRTEM and SEM images reveal that the carbon supports of Ni$_1$-NCNT and Ni$_2$-NCNT inherited the morphology of CNTs (Figs. 1a, c, S9a and S9d). In addition, elemental mapping shows an even distribution of C, N, Ni elements over the CNTs for Ni$_1$-NCNT and Ni$_2$-NCNT (Fig. S8c and

Scheme 1. Schematic illustration for the synthesis procedures of Ni$_2$-NCNT DAC and Ni-NCNT SAC.
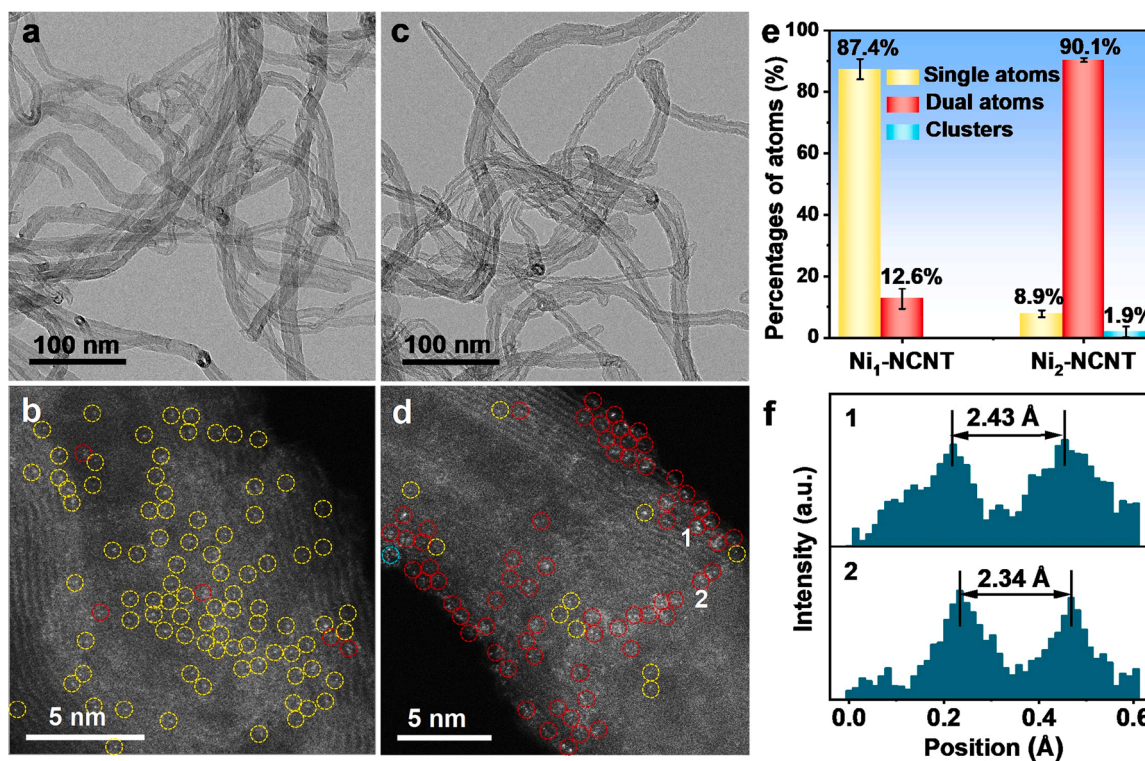

Fig. 1. . (a,c) TEM images of Ni$_1$-NCNT (a) and Ni$_2$-NCNT (c). (b,d) High-resolution HAADF-STEM images of Ni$_1$-NCNT (b) and Ni$_2$-NCNT (d), with single-atoms, dual-atoms and nanoclusters highlighted with yellow, red, and blue circles, respectively. (e) The percentages of single-atoms, dual atoms and nanoclusters in 1b and 1d. (f) Intensity profiles at the areas 1 and 2 in 1d.

S8f). The atomic-resolution HAADF-STEM images confirm the existence of rich isolated Ni single atoms in Ni$_1$-NCNT (Figs. 1b, S9a and S9b) and Ni$_2$ dual-atoms in Ni$_2$-NCNT (Fig. 1d, S9c and S9d). As shown in Figs. 1b, S9a and S9b, the Ni atoms in Ni$_1$-NCNT are mainly isolated single-atoms accompanied with a small number of dual-atoms, with the percentage of single-atoms and dual-atoms being 87.4% and 12.6%, respectively, after counting the numbers of single-atoms and dual-atoms in above three individual images (Fig. 1e). By counting the numbers of single-atoms, dual-atoms and nanoclusters in Fig. 1d, S9c and S9d, we found that 90.1% of the Ni atoms are in pairs in Ni$_2$-NCNT (Fig. 1e), much higher than those of DACs synthesized using metal salts as a precursors [59], demonstrating that our strategy can successfully achieve the controlled

synthesis of pure DACs. As shown in Fig. 1 f, the intensity profiles at areas 1 and 2 indicate that the distance between the adjacent Ni atoms is approximately 2.4 Å.

X-ray photoelectron spectroscopy (XPS) was conducted to probe the electronic state and coordination environment of Ni atom in Ni$_1$-NCNT and Ni$_2$-NCNT. As shown in Fig. S10, the binding energies of Ni 2$p_{3/2}$ (855.5 eV) in both Ni$_1$-NCNT and Ni$_2$-NCNT are higher than that of Ni^0 (853.5 eV) [60], and lower than that of Ni^{2+} (855.9 eV) [61], indicating the valence state of Ni in both Ni$_1$-NCNT and Ni$_2$-NCNT are between 0 and + 2. The high-resolution N 1 s spectra can be deconvoluted into four subpeaks at ~398.9, 399.5, 400.4, and 401.4 eV, corresponding to pyridinic N, Ni–N (pyridinic), pyrrolic N, and graphitic N, respectively

(Fig. S11) [13,62–64]. No subpeak at ~399.5 eV was found in NCNT, demonstrating that the subpeaks at 399.5 eV in Ni$_1$-NCNT and Ni$_2$-NCNT are ascribed to Ni–N. In addition, the high-resolution C 1 *s* spectra show almost identical profiles for Ni$_1$-NCNT, Ni$_2$-NCNT and NCNT (Fig. S12), suggesting no coordination between Ni and C in Ni$_1$-NCNT and Ni$_2$-NCNT.

X-ray absorption fine structure (XAFS) spectroscopy was conducted to investigate the electronic and structural information of Ni atoms in Ni$_1$-NCNT and Ni$_2$-NCNT. The energies of the pre-edges in the X-ray absorption near-edge structure (XANES) spectra for Ni$_1$-NCNT and Ni$_2$-NCNT are higher than that for Ni foil and lower than those for phthalocyanine nickel (NiPc) and NiO (Fig. 2a, Fig. S13), further indicating the valence states of Ni atoms in Ni$_1$-NCNT and Ni$_2$-NCNT are between 0 and + 2. The identifiable pre-edge peaks *a* and *b* in Fig. 2a are attributed to the Ni $1 s \rightarrow 3d$ and $1 s \rightarrow 4p_z$ transitions, respectively [65]. As shown in Fig. 2b, the main peaks are located at ~1.43 Å in Ni$_1$-NCNT and 1.36 Å in Ni$_2$-NCNT, which are close to the distance of Ni–N bond in NiPc (1.51 Å), and thus could be assigned to the Ni–N bonds. In addition, the peak at 2.30 Å in Ni$_2$-NCNT is close to that of the Ni–Ni bond (2.18 Å) in Ni foil, and this distance is also close to the Ni-Ni distance observed in the HAADF-STEM image of Ni$_2$-NCNT (Fig. 1 f), indicating the existence of Ni–Ni coordination in Ni$_2$-NCNT. A small peak around 2.30 Å is also observed in the Ni K-edge FT-EXAFS profile of Ni$_1$-NCNT (Fig. 2b and e), which can be ascribed to the Ni–Ni bonds due to the existence of 12.6% dual-atoms in Ni$_1$-NCNT (Fig. 1e). The coordination number of Ni–N is 3.7 ± 0.6 for Ni$_1$-NCNT, whereas the coordination numbers of Ni–N and Ni–Ni are 2.9 ± 0.6 and 1.1 ± 0.4 for Ni$_2$-NCNT, respectively (Table S1). To identify the coordination structure around Ni atom, Fourier-transform extended X-ray fine structure (FT-EXAFS) spectra were recorded for Ni$_1$-NCNT, Ni$_2$-NCNT and the reference samples (Fig. 2c, 2d, and S14, S15). The spectra of Ni$_1$-NCNT and Ni$_2$-NCNT were fitted in R space on the basis of optimized structural models of the SAC (Ni–N$_4$) and DAC (Ni$_2$–N$_3$) (the inset shown in Fig. 2c

and d), and the fitting curves agree well with the experimental results. To further clarify the coordination structures for the Ni species, EXAFS wavelet transform analysis was carried out (Figs. 2e, and S16). Compared with Ni$_1$-NCNT, Ni$_2$-NCNT shows not only the signals of Ni–N coordination but also the signals of Ni–Ni coordination, further confirming that the coordination structure of Ni$_2$-NCNT is Ni$_2$–N$_3$ and that of Ni$_1$-NCNT is Ni–N$_4$.

3.2. Electrocatalytic CO$_2$ reduction

The electrocatalytic CO$_2$ reduction performances were assessed with a standard three-electrode system in CO$_2$-saturated 0.5 M KHCO$_3$ electrolyte. We firstly investigated the electrocatalytic activity for CO$_2$ reduction of a physical mixture of Ni$_2$(qpyzc)$_2$ and CNTs (Fig. S17), the results reveal that H$_2$ is the only product, indicating the physical mixture of Ni$_2$(qpyzc)$_2$ and CNT do not display the electrocatalytic activity for CO$_2$ reduction. As a key point in the synthesis process, the loading of complex precursor may affect the catalytic activities of DACs. Low concentration of the precursor can evenly distribute on the surface of CNTs during the in situ synthesis process, forming DACs with good dispersion after subsequent pyrolysis. High concentration of the precursor will lead to the aggregation of the complexes through intermolecular π-π stacking, and eventually the generation of nanoparticles in the subsequent pyrolysis process, thus decrease the selectivity for CO$_2$ electroreduction. In this regard, the feed ratio of ligand H$_2$qpyzc, nickel acetate and CNT was varied to prepare diatomic Ni$_2$ catalysts with different Ni loadings. Inductively coupled plasma atomic emission spectroscopy (ICP-AES) revealed that the final Ni contents are 0.37, 0.61, 1.04, 1.85 and 1.87 wt% for 2%-Ni$_2$-NCNT, 4%-Ni$_2$-NCNT, 8%-Ni$_2$-NCNT, 12%-Ni$_2$-NCNT and 24%-Ni$_2$-NCNT catalysts (the percentages denote the mass ratios of the Ni$_2$(qpyzc)$_2$ precursor to CNT), respectively (Table S2). As shown in the XRD patterns (Fig. S18), although the Ni content increases, there are no discernible peaks
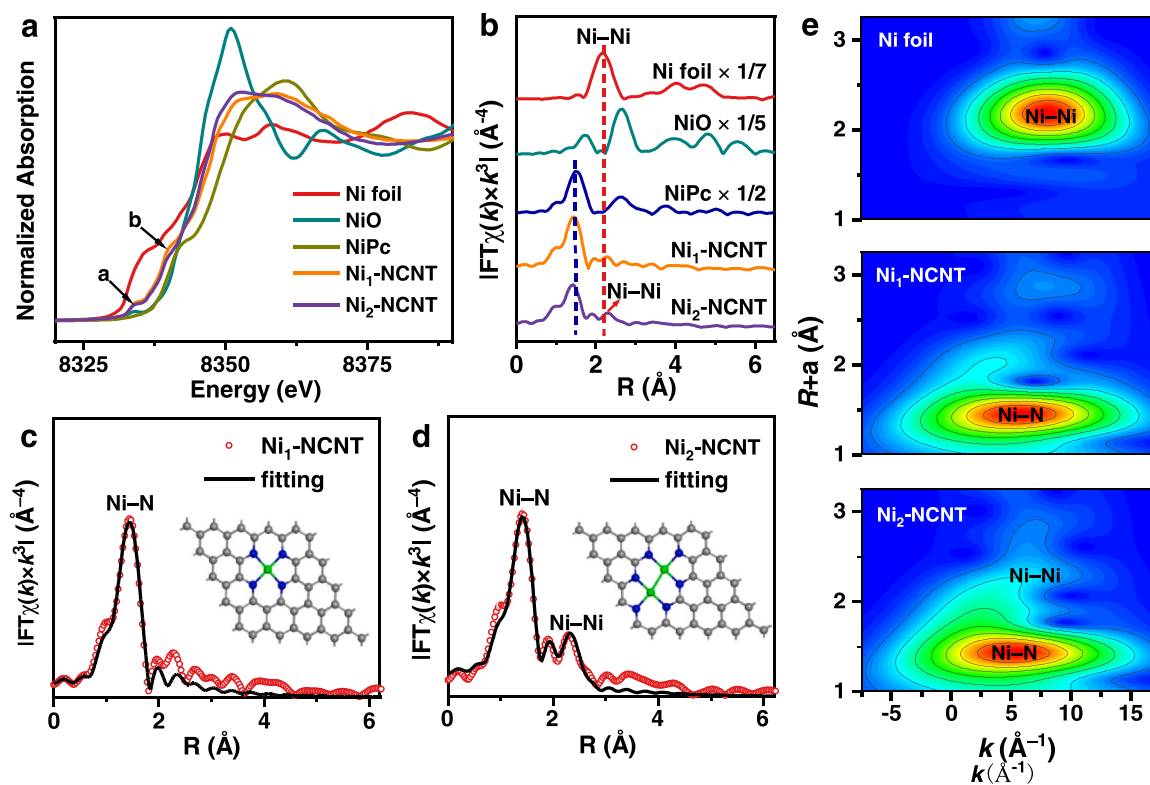

Fig. 2. (a) Ni K-edge XANES spectra of the samples. (b) Ni K-edge FT-EXAFS profiles of the samples. (c) Ni K-edge EXAFS fitting curves of Ni$_1$-NCNT in the R space, the inset showing the optimized structural model of SACs (Ni–N$_4$). (d) Ni K-edge EXAFS fitting curves of Ni$_2$-NCNT in the R space, the inset showing the optimized structural model of DAC (Ni$_2$–N$_3$). (e) Wavelet transforms of k^2-weighted EXAFS.

characteristic of metallic Ni nanoparticles for these samples after acid washing. The final Ni loadings and catalytic activities of 12%-Ni$_2$-NCNT and 24%-Ni$_2$-NCNT are very close, indicating that the loading of diatomic Ni$_2$ pairs was almost saturated when the ratio reached 12%, and further increased Ni loading in 24%-Ni$_2$-NCNT mainly forms Ni nanoparticles, which were removed by acid washing. In the performance tests, 4%-Ni$_2$-NCNT exhibits the best catalytic activity. A higher or lower mass ratio of Ni$_2$(qpyzc)$_2$/CNT would result in lower the activity of final Ni$_2$-NCNT catalyst (Fig. S19). 2%-Ni$_2$-NCNT shows inferior activity, probably owing to the lower Ni content; higher Ni contents would lead to partial agglomeration of Ni atoms to generate Ni nanoparticles (Fig. S20), resulting in a lower activity and selectivity for CO$_2$ electroreduction.

Pyrolysis temperature is another important parameter during the synthesis, and it could affect the controllable synthesis of diatomic catalysts and thus their catalytic activities. Thermogravimetric analysis (TGA) shows that the distinct weight loss of Ni$_2$(qpyzc)$_2$ starts at the temperature around 500 °C, and the weight loss could be ascribed to the decomposition of Ni$_2$(qpyzc)$_2$ (Fig. S21). Therefore, the pyrolysis temperatures were set at 500, 550, 600, 650, 700, 800, and 900 °C, respectively, and distinct XRD peaks of crystalline Ni (PDF # 04–0850) emerge when the pyrolysis temperature reaches over 800 °C (Fig. S22), revealing that higher temperature would induce agglomeration of Ni atoms. The DAC displays the highest electrocatalytic performance when the pyrolysis temperature was set at 600 °C (Fig. S23), and a higher pyrolysis temperature would cause the decrease in the CO partial current density (j_{CO}) and FE of the catalyst, particularly when Ni nanoparticles are present on CNTs. On the basis of the above experimental results, we obtained the best electrocatalytic CO$_2$RR of Ni$_2$-NCNT when the mass ratio of Ni$_2$(qpyzc)$_2$/CNT was 4% (0.61 wt% of Ni loading) and the pyrolysis temperature was 600 °C.

Then we compared the electrocatalytic CO$_2$ reduction performance of Ni$_2$-NCNT (0.61 wt% of Ni content, Table S2), Ni$_1$-NCNT (0.66 wt% of Ni content) and NCNT. CO and H$_2$ are the only gas products according to the analysis of gas chromatography (GC). Moreover, no significant liquid products were detected via ^{1}H NMR spectroscopy (Fig. S24). The electrochemical performance was first assessed via linear sweep voltammetry (LSV) at the scan rate of 2 mV s^{-1}; Ni$_2$-NCNT delivers a higher catalytic current density than Ni$_1$-NCNT and NCNT (Fig. 3a, Fig. S25).

The control potential electrolysis and GC analysis revealed that Ni$_1$-NCNT shows lower FE$_{CO}$ (87–90%) in the potential range from −0.8 V to −1.1 V vs. RHE, whereas Ni$_2$-NCNT exhibits higher FE$_{CO}$ (90–97%) over a wider potential range from −0.8 V to −1.2 V vs. RHE (Fig. 3b). For FE$_{CO}$ > 80%, the potential range for Ni$_2$-NCNT is from –0.7 to −1.4 V vs. RHE, in contrast to from –0.8 to −1.1 V for Ni$_1$-NCNT. The maximum FE$_{CO}$ for Ni$_2$-NCNT is 97%, in contrast to 89% (for Ni$_1$-NCNT) and 0.6% (for NCNT) under the same potential (–0.9 V vs. RHE). The significant difference in FE$_{CO}$ between Ni$_2$-NCNT and Ni$_1$-NCNT indicates that dual-atom site can effectively inhibit HER and thus give superior electrocatalytic activity for CO$_2$ reduction.

The difference in j_{CO} between DACs and SACs is more pronounced. A large catalytic current density of 76.2 mA cm^{-2} was obtained for Ni$_2$-NCNT at −1.4 V vs. RHE, which is much higher than that of Ni$_1$-NCNT (32.7 mA cm^{-2}) and NCNT (0.4 mA cm^{-2}) (Fig. 3c). As shown in Fig. S26, after iR correction, Ni$_2$-NCNT DAC also displays much higher j_{CO} (82.0 mA cm^{-2}) than Ni$_1$-NCNT SAC (j_{CO} = 42 mA cm^{-2}) at −1.1 V vs. RHE. These j_{CO} values are higher than those of most reported electrocatalysts for CO$_2$-to-CO conversion (Table S3), revealing that Ni$_2$-NCNT is one of the best electrocatalysts reported thus far for CO$_2$ reduction.

The charge-transfer resistance was evaluated via electrochemical impedance spectroscopy (EIS), and Ni$_2$-NCNT shows a better charge transfer efficiency than Ni$_1$-NCNT and NCNT (Fig. S27a). The Tafel slope value for Ni$_2$-NCNT (117 mV dec^{-1}) is significantly lower than that of Ni$_1$-NCNT (189 mV dec^{-1}), demonstrating a better kinetics for CO$_2$ reduction (Fig. S27b). Furthermore, the double-layer capacitance (C_{dl}) values for Ni$_2$-NCNT (5.7 mF cm^{-2}) and Ni$_1$-NCNT (5.9 mF cm^{-2}) are quite similar (Fig. S28), demonstrating that the higher catalytic activity of Ni$_2$-NCNT does not stem from a larger electrochemical active surface area (ECSA). SCN$^-$ anion is commonly used as a poisoning agent for the catalytic sites [66]. As shown in Fig. S29, the current density of Ni$_2$-NCNT is dramatically lowered after the addition of SCN$^-$, indicating the Ni$_2$ dual-atom site is the primary active site for CO$_2$ electroreduction. In order to compare the catalytic activities of Ni$_2$-NCNT and Ni$_1$-NCNT more directly, their current densities were normalized to A mg$_{Ni}^{-1}$, and more pronounced differences in catalytic activities are shown in Fig. 3d. The j_{CO} mass activity of Ni$_2$-NCNT (25.0 A mg$_{Ni}^{-1}$) is 2.3-times higher than that of Ni$_1$-NCNT (10.9 A mg$_{Ni}^{-1}$), confirming that the enhanced
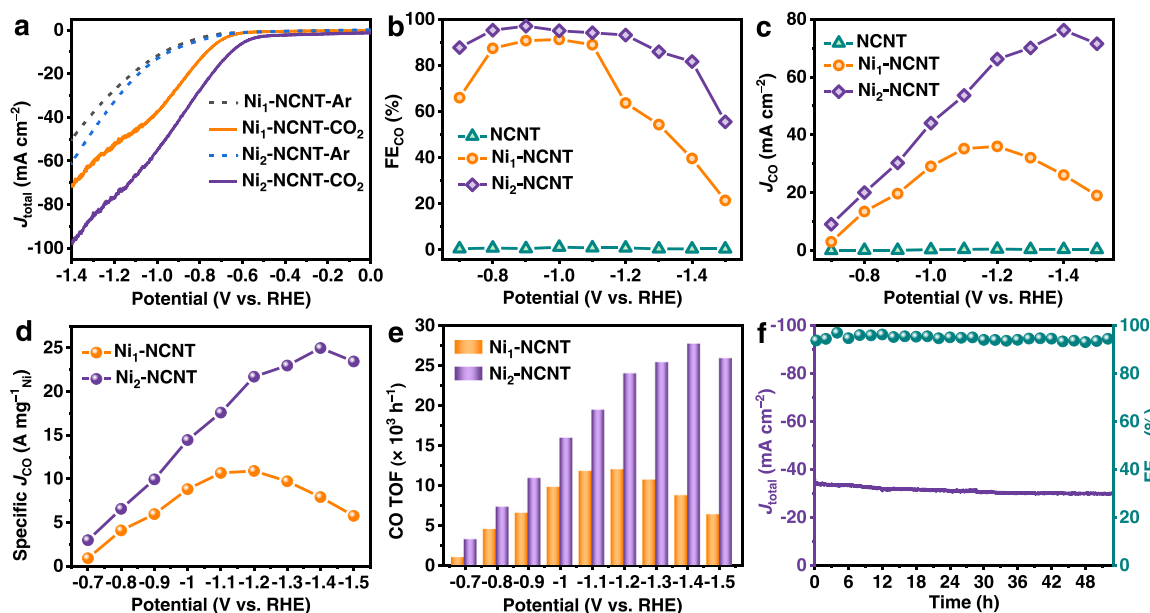

Fig. 3. (a) LSV curves in Ar- or CO$_2$-saturated 0.5 M KHCO$_3$ electrolyte. (b, c) FE$_{CO}$ (b) and CO partial current density (c) for NCNT, Ni$_1$-NCNT and Ni$_2$-NCNT catalysts. (d) The specific current densities of CO normalized by the mass of Ni for Ni$_1$-NCNT and Ni$_2$-NCNT. (e) TOFs for Ni$_1$-NCNT and Ni$_2$-NCNT at different potentials. (f) Chrono-amperometry curve and FE$_{CO}$ for Ni$_2$-NCNT at −0.9 V vs. RHE. All the data were measured without the iR correction.

catalytic activity of Ni_2-NCNT originates from its dual-atom synergistic effect rather than the different Ni loading. The turnover frequencies (TOFs) for CO_2 reduction were calculated to evaluate the intrinsic activity of single Ni sites, and Ni_2-NCNT gives a high TOF value of $2.75 \times 10^4 \ h^{-1}$ at -1.4 V, much higher than that of Ni_1-NCNT ($1.19 \times 10^4 \ h^{-1}$ at -1.2 V) (Fig. 3e). In addition, Ni_2-NCNT exhibits a good stability, with the Faraday efficiency remaining constant within 52 h continuous electrolysis (Fig. 3f). The results of XPS measurements demonstrate that the valence states of Ni atoms before and after the catalysis are the same (Fig. S30), further demonstrating the good stability of Ni_2-NCNT. To further evaluate the intrinsic electrocatalytic activity of Ni_2-NCNT, electrocatalytic CO_2 reduction activity and selectivity were investigated in a flow cell with 1.0 M $KHCO_3$ electrolyte (Fig. S31). As shown in Fig. S31, the CO Faraday efficiency (FE_{CO}) of Ni_2-NCNT maintains over 93.4% even at a high current density of 250 mA cm^{-2}, this value is much higher than that of reported Ni_2 DAC (with a FE_{CO} of ~86% at a current density of 200 mA cm^{-2}) [46], further demonstrating the outstanding activity and selectivity of as-prepared Ni_2-NCNT DAC for electrocatalytic CO_2 reduction.

3.3. Diatomic synergistic mechanism

In order to further unveil the mechanism of CO_2RR and the activity difference between Ni_2-NCNT and Ni_1-NCNT, the density functional theory (DFT) calculations were performed. Two optimized DAC models of Ni_2-N_4 and Ni_2-N_3 (Ni_2-NCNT), as well as two related SAC models of Ni-N_4 (Ni_1-NCNT) and Ni-N_3 were constructed for comparison (Fig. 4a, and S32, S33). As shown in Fig. 4b, the CO_2 electroreduction to CO involves four elementary steps: (1) $CO_2 + * \rightarrow *CO_2$ (* = catalytic site); (2) $*CO_2 + H^+ + e^- \rightarrow *COOH$; (3) $*COOH + H^+ + e^- \rightarrow *CO + H_2O$; (4) $*CO \rightarrow CO + *$. The calculated Gibbs free energy diagrams for these four steps are shown in Fig. 4c. For CO_2 adsorption and proton-coupled electron transfer (PCET) steps, Ni-N_4, Ni_2-N_4, Ni_2-N_3 and Ni-N_3 exhibit the free energy changes (ΔG) of 1.65 eV, 1.64 eV, 0.76 eV and -0.06 eV, respectively, in which Ni-N_3 shows the most favorable ΔG for the formation of adsorbed *COOH intermediate. Subsequently, the *COOH intermediate undergoes the second PCET, forming a water molecule and *CO, and the free energy change for this step over the four

model catalysts are all downhill. Finally, the *CO desorbs from the catalysts and releases the active site. For Ni-N_3 and Ni_2-N_3, the *CO desorption step is endothermic with a free energy change of 1.26 eV and 0.21 eV, respectively. While for Ni-N_4 and Ni_2-N_4, the *CO desorption step is spontaneous with a free energy change of -0.62 eV and -0.56 eV, respectively. According to our calculations, the formation of the *COOH intermediate is regarded as the rate-determining step (RDS) for Ni-N_4, Ni_2-N_4 and Ni_2-N_3, whereas the desorption of the *CO intermediate is the RDS for Ni-N_3. Among the four model catalysts, the Ni_2-N_3 exhibits the superior CO_2 reduction activity with a free energy change of 0.76 eV in the rate-determining step, the synergistic effect between two Ni atoms in Ni_2-N_3 can stabilize the *COOH intermediate and obviously lower the free energy change in the RDS compared with that of Ni-N_4 SAC (1.65 eV). Therefore, the Ni_2-N_3 exhibits the best electrocatalytic activity for CO_2 reduction, which is consistent with the experimental results.

4. Conclusions

In summary, we have developed an effective strategy for controlled synthesis of a Ni_2 dual-atom catalyst as well as a Ni_1 single-atom catalyst by modulating the ligands of the precursors. The effects of precursor concentration and pyrolysis temperature on controlled synthesis and catalytic activity of Ni_2-NCNT DAC were investigated. Excessively high concentration of the dinuclear complex precursor and high pyrolysis temperature would lead to the agglomeration of Ni atoms, thus lowering the CO_2 reduction catalytic activity and selectivity. The optimized Ni_2-NCNT DAC with diatomic synergy exhibits excellent electrocatalytic activity and stability for electrocatalytic CO_2 reduction, achieving a high current density of 76 mA cm^{-2} and a high Faradaic efficiency of 97%. DFT calculations confirm that the diatomic Ni_2-N_3 structure of Ni_2-NCNT can enhance the catalytic activity by lowering the reaction free energy via the formation of a bridged *COOH intermediate at Ni_2 catalytic site. Our work not only provides an ideal strategy for precise and controlled synthesis of DACs, but also clarifies the intrinsic origin of the superior activity of dual-atom Ni_2 electrocatalyst toward CO_2RR.
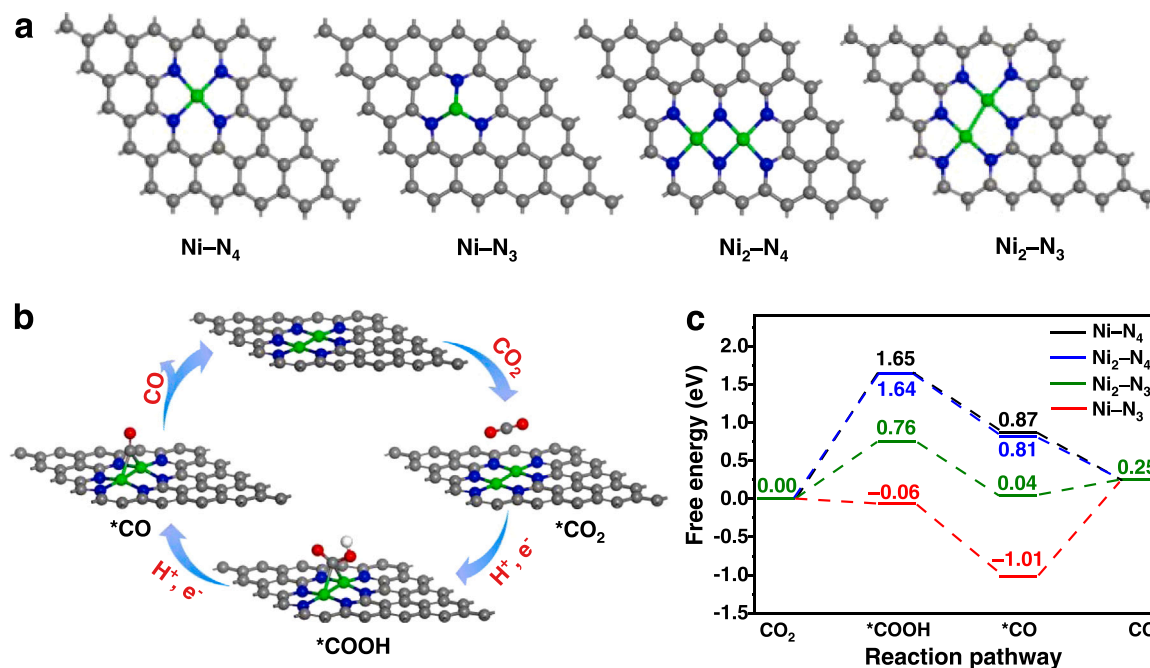

Fig. 4. (a) The structural models of Ni-N_4 (Ni_1-NCNT) and Ni-N_3 SACs, as well as Ni_2-N_4 and Ni_2-N_3 (Ni_2-NCNT) DACs. (b) The proposed reaction pathways of Ni_2-N_3 (Ni_2-NCNT) for CO_2 electroreduction to CO. (c) Calculated free energy diagram for the conversion of CO_2 to CO.

CRediT authorship contribution statement

Xiang-Ming Liang: Writing – original draft. **Hong-Juan Wang:** Investigation. **Chao Zhang:** Writing – review & editing. **Di-Chang Zhong:** Formal analysis. **Tong-Bu Lu:** Supervision, Writing – review & editing.

Declaration of Competing Interest

The authors declare that they have no known competing financial interests or personal relationships that could have appeared to influence the work reported in this paper.

Data availability

Data will be made available on request.

Appendix A. Supporting information

Supplementary data associated with this article can be found in the online version at doi:10.1016/j.apcatb.2022.122073.

References

[1] C.W. Li, J. Ciston, M.W. Kanan, Electroreduction of carbon monoxide to liquid fuel on oxide-derived nanocrystalline copper, Nature 508 (2014) 504–507.
[2] J. Qiao, Y. Liu, F. Hong, J. Zhang, A review of catalysts for the electroreduction of carbon dioxide to produce low-carbon fuels, Chem. Soc. Rev. 43 (2014) 631–675.
[3] F. Pan, W. Deng, C. Justiniano, Y. Li, Identification of champion transition metals centers in metal and nitrogen-codoped carbon catalysts for CO₂ reduction, Appl. Catal. B Environ. 226 (2018) 463–472.
[4] S. Gao, Y. Lin, X. Jiao, Y. Sun, Q. Luo, W. Zhang, D. Li, J. Yang, Y. Xie, Partially oxidized atomic cobalt layers for carbon dioxide electroreduction to liquid fuel, Nature 529 (2016) 68–71.
[5] Y. Zheng, A. Vasileff, X. Zhou, Y. Jiao, M. Jaroniec, S.Z. Qiao, Understanding the roadmap for electrochemical reduction of CO₂ to multi-carbon oxygenates and hydrocarbons on copper-based catalysts, J. Am. Chem. Soc. 141 (2019) 7646–7659.
[6] A. Vasileff, Y. Zheng, S.Z. Qiao, Carbon solving carbon's problems: recent progress of nanostructured carbon-based catalysts for the electrochemical reduction of CO₂, Adv. Energy Mater. 7 (2017) 1700759.
[7] S.F. Tang, X.L. Lu, C. Zhang, Z.W. Wei, R. Si, T.B. Lu, Decorating graphdiyne on ultrathin bismuth subcarbonate nanosheets to promote CO₂ electroreduction to formate, Sci. Bull. 66 (2021) 1533–1541.
[8] Z. Yang, H. Wang, X. Fei, W. Wang, Y. Zhao, X. Wang, X. Tan, Q. Zhao, H. Wang, J. Zhu, L. Zhou, H. Ning, M. Wu, MOF derived bimetallic CuBi catalysts with ultra-wide potential window for high-efficient electrochemical reduction of CO₂ to formate, Appl. Catal. B Environ. 298 (2021), 120571.
[9] X. Ma, J. Du, H. Sun, F. Ye, X. Wang, P. Xu, C. Hu, L. Zhang, D. Liu, Boron, nitrogen co-doped carbon with abundant mesopores for efficient CO₂ electroreduction, Appl. Catal. B Environ. 298 (2021), 120543.
[10] B. Liu, Y. Xie, X. Wang, C. Gao, Z. Chen, J. Wu, H. Meng, Z. Song, S. Du, Z. Ren, Copper-triggered delocalization of bismuth p-orbital favours high-throughput CO₂ electroreduction, Appl. Catal. B Environ. 301 (2022), 120781.
[11] M. Li, Y. Ma, J. Chen, R. Lawrence, W. Luo, M. Sacchi, W. Jiang, J. Yang, Residual chlorine induced cationic active species on a porous copper electrocatalyst for highly stable electrochemical CO₂ reduction to C₂₊, Angew. Chem. Int. Ed. 60 (2021) 11487–11493.
[12] X. Meng, J. Yang, C. Zhang, Y. Fu, K. Li, M. Sun, X. Wang, C. Dong, B. Ma, Y. Ding, Light-driven CO₂ reduction over prussian blue analogues as heterogeneous catalysts, ACS Catal. 12 (2021) 89–100.
[13] Y.N. Gong, B.Z. Shao, J.H. Mei, W. Yang, D.C. Zhong, T.B. Lu, Facile synthesis of C₃N₄-supported metal catalysts for efficient CO₂ photoreduction, Nano Res. 15 (2021) 551–556.
[14] J.H. Zhang, Y.N. Gong, H.J. Wang, Y.C. Wang, W. Yang, J.H. Mei, D.C. Zhong, T. B. Lu, Ordered heterogeneity of molecular photosensitizer toward enhanced photocatalysis, Proc. Natl. Acad. Sci. USA 119 (2022), e2118278119.
[15] J. Yang, Z. Qiu, C. Zhao, W. Wei, W. Chen, Z. Li, Y. Qu, J. Dong, J. Luo, Z. Li, Y. Wu, In situ thermal atomization to convert supported nickel nanoparticles into surface-bound nickel single-atom catalysts, Angew. Chem. Int. Ed. 57 (2018) 14095–14100.
[16] C. Zhao, X. Dai, T. Yao, W. Chen, X. Wang, J. Wang, J. Yang, S. Wei, Y. Wu, Y. Li, Ionic exchange of metal-organic frameworks to access single nickel sites for efficient electroreduction of CO₂, J. Am. Chem. Soc. 139 (2017) 8078–8081.
[17] X.M. Hu, H.H. Hval, E.T. Bjerglund, K.J. Dalgaard, M.R. Madsen, M.M. Pohl, E. Welter, P. Lamagni, K.B. Buhl, M. Bremholm, M. Beller, S.U. Pedersen, T. Skrydstrup, K. Daasbjerg, Selective CO₂ reduction to CO in water using earth-abundant metal and nitrogen-doped carbon electrocatalysts, ACS Catal. 8 (2018) 6255–6264.
[18] X. Wang, Z. Chen, X. Zhao, T. Yao, W. Chen, R. You, C. Zhao, G. Wu, J. Wang, W. Huang, J. Yang, X. Hong, S. Wei, Y. Wu, Y. Li, Regulation of coordination number over single Co sites: triggering the efficient electroreduction of CO₂, Angew. Chem. Int. Ed. 57 (2018) 1962–1966.
[19] X. Rong, H.J. Wang, X.L. Lu, R. Si, T.B. Lu, Controlled synthesis of a vacancy-defect single-atom catalyst for boosting CO₂ electroreduction, Angew. Chem. Int. Ed. 59 (2020) 1961–1965.
[20] J. Gu, C.-S. Hsu, L. Bai, H.M. Chen, X. Hu, Atomically dispersed Fe³⁺ sites catalyze efficient CO₂ electroreduction to CO, Science 364 (2019) 1091–1094.
[21] C. Zhao, Y. Wang, Z. Li, W. Chen, Q. Xu, D. He, D. Xi, Q. Zhang, T. Yuan, Y. Qu, J. Yang, F. Zhou, Z. Yang, X. Wang, J. Wang, J. Luo, Y. Li, H. Duan, Y. Wu, Y. Li, Solid-diffusion synthesis of single-atom catalysts directly from bulk metal for efficient CO₂ reduction, Joule 3 (2019) 584–594.
[22] H. Fei, J. Dong, Y. Feng, C.S. Allen, C. Wan, B. Volosskiy, M. Li, Z. Zhao, Y. Wang, H. Sun, P. An, W. Chen, Z. Guo, C. Lee, D. Chen, I. Shakir, M. Liu, T. Hu, Y. Li, A. I. Kirkland, X. Duan, Y. Huang, General synthesis and definitive structural identification of MN₄C₄ single-atom catalysts with tunable electrocatalytic activities, Nat. Catal. 1 (2018) 63–72.
[23] X.P. Yin, H.J. Wang, S.F. Tang, X.L. Lu, M. Shu, R. Si, T.B. Lu, Engineering the coordination environment of single-atom platinum anchored on graphdiyne for optimizing electrocatalytic hydrogen evolution, Angew. Chem. Int. Ed. 57 (2018) 9382–9386.
[24] X. Guo, G. Fang, G. Li, H. Ma, H. Fan, L. Yu, C. Ma, X. Wu, D. Deng, M. Wei, D. Tan, R. Si, S. Zhang, J. Li, L. Sun, Z. Tang, X. Pan, X. Bao, Direct, nonoxidative conversion of methane to ethylene, aromatics, and hydrogen, Science 344 (2014) 616–619.
[25] H. Guo, D.H. Si, H.J. Zhu, Q.X. Li, Y.B. Huang, R. Cao, Ni single-atom sites supported on carbon aerogel for highly efficient electroreduction of carbon dioxide with industrial current densities, eScience 2 (2022) 295–303.
[26] Y. Guo, S. Yao, Y. Xue, X. Hu, H. Cui, Z. Zhou, Nickel single-atom catalysts intrinsically promoted by fast pyrolysis for selective electroreduction of CO₂ into CO, Appl. Catal. B Environ. 304 (2022), 120997.
[27] Y. Hou, Y.L. Liang, P.C. Shi, Y.B. Huang, R. Cao, Atomically dispersed Ni species on N-doped carbon nanotubes for electroreduction of CO₂ with nearly 100% CO selectivity, Appl. Catal. B Environ. 271 (2020), 118929.
[28] H. Xu, Y. Ma, J. Chen, W.X. Zhang, J. Yang, Electrocatalytic reduction of nitrate - a step towards a sustainable nitrogen cycle, Chem. Soc. Rev. 51 (2022) 2710–2758.
[29] F. Calle-Vallejo, D. Loffreda, M.T. Koper, P. Sautet, Introducing structural sensitivity into adsorption-energy scaling relations by means of coordination numbers, Nat. Chem. 7 (2015) 403–410.
[30] X. Hong, K. Chan, C. Tsai, J.K. Nørskov, How doped MoS₂ breaks transition-metal scaling relations for CO₂ electrochemical reduction, ACS Catal. 6 (2016) 4428–4437.
[31] W. Ren, X. Tan, X. Chen, G. Zhang, K. Zhao, W. Yang, C. Jia, Y. Zhao, S.C. Smith, C. Zhao, Confinement of ionic liquids at single-Ni-sites boost electroreduction of CO₂ in aqueous electrolytes, ACS Catal. 10 (2020) 13171–13178.
[32] Y. Ying, X. Luo, J. Qiao, H. Huang, "More is different:" synergistic effect and structural engineering in double-atom catalysts, Adv. Funct. Mater. 31 (2020) 2007423.
[33] R. Li, D. Wang, Understanding the structure-performance relationship of active sites at atomic scale, Nano Res. 15 (2022) 6888–6923.
[34] Y. Zhao, K.R. Yang, Z. Wang, X. Yan, S. Cao, Y. Ye, Q. Dong, X. Zhang, J.E. Thorne, L. Jin, K.L. Materna, A. Trimpalis, H. Bai, S.C. Fakra, X. Zhong, P. Wang, X. Pang, J. Guo, M. Flytzani-Stephanopoulos, G.W. Brudvig, V.S. Batista, D. Wang, Stable iridium dinuclear heterogeneous catalysts supported on metal-oxide substrate for solar water oxidation, Proc. Natl. Acad. Sci. USA 115 (2018) 2902–2907.
[35] Y. Pan, C. Zhang, Z. Liu, C. Chen, Y. Li, Structural regulation with atomic-level precision: from single-atomic site to diatomic and atomic interface catalysis, Matter 2 (2020) 78–110.
[36] H. Rong, S. Ji, J. Zhang, D. Wang, Y. Li, Synthetic strategies of supported atomic clusters for heterogeneous catalysis, Nat. Commun. 11 (2020) 5884.
[37] S. Zhang, L. Nguyen, J.X. Liang, J. Shan, J.J. Liu, A.I. Frenkel, A. Patolla, W. Huang, J. Li, F.F. Tao, Catalysis on singly dispersed bimetallic sites, Nat. Commun. 6 (2015) 7938.
[38] Y. Li, C. Chen, R. Cao, Z. Pan, H. He, K. Zhou, Dual-atom Ag₂/graphene catalyst for efficient electroreduction of CO₂ to CO, Appl. Catal. B Environ. 268 (2020), 118747.
[39] P. Zhou, X. Hou, Y. Chao, W. Yang, W. Zhang, Z. Mu, J. Lai, F. Lv, K. Yang, Y. Liu, J. Li, J. Ma, J. Luo, S. Guo, Synergetic interaction between neighboring platinum and ruthenium monomers boosts CO oxidation, Chem. Sci. 10 (2019) 5898–5905.
[40] S. Tian, Q. Fu, W. Chen, Q. Feng, Z. Chen, J. Zhang, W.C. Cheong, R. Yu, L. Gu, J. Dong, J. Luo, C. Chen, Q. Peng, C. Draxl, D. Wang, Y. Li, Carbon nitride supported Fe₂ cluster catalysts with superior performance for alkene epoxidation, Nat. Commun. 9 (2018) 2353.

[41] W. Ren, X. Tan, W. Yang, C. Jia, S. Xu, K. Wang, S.C. Smith, C. Zhao, Isolated diatomic Ni-Fe metal-nitrogen sites for synergistic electroreduction of CO₂, Angew, Chem., Int. Ed. 58 (2019) 6972–6976.

[42] X. Lv, W. Wei, B. Huang, Y. Dai, T. Frauenheim, High-throughput screening of synergistic transition metal dual-atom catalysts for efficient nitrogen fixation, Nano Lett. 21 (2021) 1871–1878.

[43] H. Li, L. Wang, Y. Dai, Z. Pu, Z. Lao, Y. Chen, M. Wang, X. Zheng, J. Zhu, W. Zhang, R. Si, C. Ma, J. Zeng, Synergetic interaction between neighbouring platinum monomers in CO₂ hydrogenation, Nat. Nanotechnol. 13 (2018) 411–417.

[44] J. Jiao, R. Lin, S. Liu, W.C. Cheong, C. Zhang, Z. Chen, Y. Pan, J. Tang, K. Wu, S. F. Hung, H.M. Chen, L. Zheng, Q. Lu, X. Yang, B. Xu, H. Xiao, J. Li, D. Wang, Q. Peng, C. Chen, Y. Li, Copper atom-pair catalyst anchored on alloy nanowires for selective and efficient electrochemical reduction of CO₂, Nat. Chem. 11 (2019) 222–228.

[45] J. Zhang, Y. Wang, H. Wang, D. Zhong, T. Lu, Enhancing photocatalytic performance of metal-organic frameworks for CO₂ reduction by a bimetallic strategy, Chin. Chem. Lett. 33 (2022) 2065–2068.

[46] T. Ding, X. Liu, Z. Tao, T. Liu, T. Chen, W. Zhang, X. Shen, D. Liu, S. Wang, B. Pang, D. Wu, L. Cao, L. Wang, T. Liu, Y. Li, H. Sheng, M. Zhu, T. Yao, Atomically precise dinuclear site active toward electrocatalytic CO₂ reduction, J. Am. Chem. Soc. 143 (2021) 11317–11324.

[47] T. Ouyang, H.J. Wang, H.H. Huang, J.W. Wang, S. Guo, W.J. Liu, D.C. Zhong, T. B. Lu, Dinuclear metal synergistic catalysis boosts photochemical CO₂-to-CO conversion, Angew. Chem. Int. Ed. 57 (2018) 16480–16485.

[48] T. Ouyang, H.H. Huang, J.W. Wang, D.C. Zhong, T.B. Lu, A Dinuclear, Cobalt cryptate as a homogeneous photocatalyst for highly selective and efficient visible-light driven CO₂ reduction to CO in CH₃CN/H₂O solution, Angew. Chem. Int. Ed. 56 (2017) 738–743.

[49] L. Zhang, R. Si, H. Liu, N. Chen, Q. Wang, K. Adair, Z. Wang, J. Chen, Z. Song, J. Li, M.N. Banis, R. Li, T.K. Sham, M. Gu, L.M. Liu, G.A. Botton, X. Sun, Atomic layer deposited Pt-Ru dual-metal dimers and identifying their active sites for hydrogen evolution reaction, Nat. Commun. 10 (2019) 4936.

[50] H. Yan, Y. Lin, H. Wu, W. Zhang, Z. Sun, H. Cheng, W. Liu, C. Wang, J. Li, X. Huang, T. Yao, J. Yang, S. Wei, J. Lu, Bottom-up precise synthesis of stable platinum dimers on graphene, Nat. Commun. 8 (2017) 1070.

[51] X. Zheng, B. Li, Q. Wang, D. Wang, Y. Li, Emerging low-nuclearity supported metal catalysts with atomic level precision for efficient heterogeneous catalysis, Nano Res. 15 (2022) 7806–7839.

[52] T. Chao, X. Luo, W. Chen, B. Jiang, J. Ge, Y. Lin, G. Wu, X. Wang, Y. Hu, Z. Zhuang, Y. Wu, X. Hong, Y. Li, Atomically dispersed copper-platinum dual sites alloyed with palladium nanorings catalyze the hydrogen evolution reaction, Angew. Chem. Int. Ed. 56 (2017) 16047–16051.

[53] J. Pei, T. Wang, R. Sui, X. Zhang, D. Zhou, F. Qin, X. Zhao, Q. Liu, W. Yan, J. Dong, L. Zhang, Q. Li, J. Mao, W. Zhu, W. Chen, Z. Zhuang, N-bridged Co–N–Ni: new bimetallic sites for promoting electrochemical CO₂ reduction, Energy Environ. Sci. 14 (2021) 3019–3028.

[54] J. Wang, Z. Huang, W. Liu, C. Chang, H. Tang, Z. Li, W. Chen, C. Jia, T. Yao, S. Wei, Y. Wu, Y. Li, Design of N-coordinated dual-metal sites: a stable and active Pt-free catalyst for acidic oxygen reduction reaction, J. Am. Chem. Soc. 139 (2017) 17281–17284.

[55] G. Yang, J. Zhu, P. Yuan, Y. Hu, G. Qu, B.A. Lu, X. Xue, H. Yin, W. Cheng, J. Cheng, W. Xu, J. Li, J. Hu, S. Mu, J.N. Zhang, Regulating Fe-spin state by atomically dispersed Mn-N in Fe-N-C catalysts with high oxygen reduction activity, Nat. Commun. 12 (2021) 1734.

[56] W. Ye, S. Chen, Y. Lin, L. Yang, S. Chen, X. Zheng, Z. Qi, C. Wang, R. Long, M. Chen, J. Zhu, P. Gao, L. Song, J. Jiang, Y. Xiong, Precisely tuning the number of Fe atoms in clusters on N-doped carbon toward acidic oxygen reduction reaction, Chem 5 (2019) 2865–2878.

[57] N. Zhang, X. Zhang, Y. Kang, C. Ye, R. Jin, H. Yan, R. Lin, J. Yang, Q. Xu, Y. Wang, Q. Zhang, L. Gu, L. Liu, W. Song, J. Liu, D. Wang, Y. Li, A supported Pd₂ dual-atom site catalyst for efficient electrochemical CO₂ reduction, Angew. Chem. Int. Ed. 60 (2021) 13388–13393.

[58] G. Mohammadnezhad, N. Ahfad, S. Meghdadi, H. Farrokhpour, S. Schmitz, A. Haseloer, A. Buchholz, W. Plass, A. Klein, Dinuclear nickel(II) and copper(II) complexes of 8–quinoline-1H-pyrazole-3–carboxamide: crystal structure, magnetic properties, and DFT calculations, Eur. J. Inorg. Chem. 2021 (2021) 1786–1795.

[59] W. Zhu, L. Zhang, S. Liu, A. Li, X. Yuan, C. Hu, G. Zhang, W. Deng, K. Zang, J. Luo, Y. Zhu, M. Gu, Z.J. Zhao, J. Gong, Enhanced CO₂ electroreduction on neighboring Zn/Co monomers by electronic effect, Angew. Chem. Int. Ed. 59 (2020) 12664–12668.

[60] H.B. Yang, S.-F. Hung, S. Liu, K. Yuan, S. Miao, L. Zhang, X. Huang, H.-Y. Wang, W. Cai, R. Chen, J. Gao, X. Yang, W. Chen, Y. Huang, H.M. Chen, C.M. Li, T. Zhang, B. Liu, Atomically dispersed Ni(I) as the active site for electrochemical CO₂ reduction, Nat. Energy 3 (2018) 140–147.

[61] Y. Li, X. Tan, R.K. Hocking, X. Bo, H. Ren, B. Johannessen, S.C. Smith, C. Zhao, Implanting Ni-O-VOx sites into Cu-doped Ni for low-overpotential alkaline hydrogen evolution, Nat. Commun. 11 (2020) 2720.

[62] K. Tian, J. Wang, L. Cao, W. Yang, W. Guo, S. Liu, W. Li, F. Wang, X. Li, Z. Xu, Z. Wang, H. Wang, Y. Hou, Single-site pyrrolic-nitrogen-doped sp(2)-hybridized carbon materials and their pseudocapacitance, Nat. Commun. 11 (2020) 3884.

[63] J. Jiao, N.N. Zhang, L. Zhang, Q. Wang, N. Sun, Y. Pan, C. Chen, J. Li, M. Tan, R. Cui, Z. Shi, J. Zhang, H. Xiao, T. Lu, Doping ruthenium into metal matrix for promoted pH-universal hydrogen evolution, Adv. Sci. 9 (2022), e2200010.

[64] J. Jiao, Y. Pan, B. Wang, W. Yang, S. Liu, C. Zhang, Melamine-assisted pyrolytic synthesis of bifunctional cobalt-based core–shell electrocatalysts for rechargeable zinc–air batteries, J. Energy Chem. 53 (2021) 364–371.

[65] T. Yamamoto, Assignment of pre-edge peaks in K-edge x-ray absorption spectra of 3d transition metal compounds: electric dipole or quadrupole? X-Ray Spectrum. 37 (2008) 572–584.

[66] X. Li, W. Bi, M. Chen, Y. Sun, H. Ju, W. Yan, J. Zhu, X. Wu, W. Chu, C. Wu, Y. Xie, Exclusive Ni-N₄ sites realize near-unity CO selectivity for electrochemical CO₂ reduction, J. Am. Chem. Soc. 139 (2017) 14889–14892.